Tailoring Spacer Cations for Enhanced Out-of-Plane Charge Transport in 2D Layered Perovskites

Xiangjiao Du,[1†] Pingzhi Zhang,[1†] Jiayi Ma,[1] Wei Wei,[2] Chunying Rong,[3] Jiajia Wang,[1*] and Wei Li[1*]

[1]School of Chemistry and Materials Science, Hunan Agricultural University, Changsha 410128, China

[2]Institute of Theoretical Chemistry, College of Chemistry, Jilin University, Changchun 130023, China

[3]Key Laboratory of Light Energy Conversion Materials of Hunan Province College, Hunan Normal University, Changsha 410081, Hunan, China

*Emails:
weili@hunau.edu.cn (W. L.)
jiajiawang@hunau.edu.cn (J.J.W.)

† Both authors contributed equally

Communications in Computational Chemistry

ABSTRACT

Two-dimensional (2D) perovskites are promising for optoelectronic applications; however, a fundamental understanding of how organic spacer cations govern vertical charge transport remains elusive. Here, we employ a first-principles framework that combines ab initio molecular dynamics, projection-operator diabatization, and semiclassical Marcus theory to elucidate the effect of spacer cation isomerism. We show that isomerization of the carbon backbone from linear n-butylammonium to branched iso-butylammonium significantly enhances out-of-plane charge transfer rates and carrier mobilities. This enhancement originates from a synergistic interplay between interlayer spacing and dynamic structural fluctuations. The branched spacer shortens the effective carbon chain, leading to decreased interlayer separation and an increase in interlayer electronic coupling. Meanwhile, weaker hydrogen-bonding interactions between the spacer cation and the inorganic framework induce enhanced thermal fluctuations of the Pb–Br lattice, resulting in stronger diabatic energy level fluctuation and only a moderate increase in reorganization energy. Consequently, the gain in electronic coupling outweighs the increase in reorganization energy, yielding substantially higher Marcus charge transfer rates in the branched spacer system. These findings reveal carbon-chain isomerism as a key design strategy for promoting interlayer charge transport and provide guiding principles for the development of high-performance 2D perovskite optoelectronic materials.

Communications in Computational Chemistry

1. Introduction

Three-dimensional (3D) metal halide perovskite solar cells have undergone remarkable progress in recent years, with power conversion efficiencies (PCEs) rapidly increasing to certified values of up to ~27%.[1,2] However, their practical application remains limited by intrinsic instability under light, heat, and moisture, which hinders large scale commercialization.[3–10] In this context, two-dimensional (2D) perovskites have emerged as promising alternatives owing to their superior environmental stability and unique photophysical properties.[11–18] These materials have demonstrated considerable potential as active components in photodetectors, light-emitting diodes, and solar cells.[19–25] The general formula of 2D Ruddlesden-Popper (RP) perovskites is $(R\text{-}NH_3)_2(A)_{n-1}M_nX_{3n+1}$, where $R\text{-}NH_3$ denotes a bulky ammonium spacer cation, A is a small monovalent cation occupying the perovskite cage, M is a divalent metal cation, X is a halide anion, and n represents the number of $[MX_6]^{4-}$ octahedral layers. Structurally, the inorganic slabs act as potential wells, while the organic spacer layers serve as insulating barriers, giving rise to natural multiple quantum well architectures. The enhanced stability of 2D RP perovskites primarily arises from the hydrophobic nature of the organic spacer layers that effectively prevents the penetration of moisture into the perovskite lattice. Despite these advantages, the PCE of 2D RP perovskite solar cells remains around 20%,[26–30] still lagging behind their 3D counterparts. This limitation is largely attributed to inefficient interlayer charge transport caused by the insulating nature of the organic spacer layers. Therefore, improving interlayer charge transfer in 2D perovskites is of fundamental importance for advancing high-performance optoelectronic devices based on these materials.

A number of studies have focused on improving interlayer charge transport in 2D RP perovskites through chemical modification of both organic and inorganic components, including tunning the carbon chain length, fluorination of spacer cations, and varying the thickness of inorganic layers, etc.[31–39] These pioneer efforts certainly promote the flourishing development of RP perovskites. In this work, we elucidate how isomerism of organic spacer cations influences out-of-plane charge transport in 2D RP perovskites, using a computational framework that combines *ab initio* molecular dynamics (AIMD), projection-operator diabatization (POD), and semiclassical Marcus theory, as developed in our group.[32,40] We focus on $n = 2$ RP perovskites incorporating linear *n*-butylammonium (*n*-BA) and its branched isomer, iso-butylammonium (iso-BA). Our simulations reveal that the iso-BA system exhibits significantly enhanced out-of-plane carrier mobilities compared to its *n*-BA counterpart. In particular, iso-BA introduces weaker hydrogen-bonding interactions between the organic spacer cation and the inorganic framework, which increase lattice fluctuations and thus moderately raise the reorganization energy. Concurrently, the shortened effective carbon chain length reduces the interlayer spacing, leading to a substantial enhancement in interlayer electronic coupling. The gain in electronic coupling outweighs the increase in reorganization energy, resulting in electron and hole mobilities that are order of magnitude higher than those in the *n*-BA system. These findings provide fundamental

insights into the structure-transport relationship governing out-of-plane charge transfer in 2D layered perovskites and offer design principles for high-performance 2D optoelectronic materials.

2. Methods

All geometric optimizations, electronic structure calculations, and AIMD simulations were performed using the VASP code.[41,42] The interaction between valence electrons and ionic cores were described using the projector augmented-wave (PAW) method. Electronic exchange-correlation effects were treated within the generalized gradient approximation of Perdew-Burke-Ernzerhof (PBE) functional.[43,44] Dispersion interactions were accounted for using the DFT-D3 scheme with Becke–Johnson damping.[45,46] A plane-wave kinetic energy cutoff of 400 eV was employed. Brillouin-zone integrations were performed on Γ-centered Monkhorst-Pack *k*-point meshes of 4×4×1. Structural optimizations were performed until the energy and force convergence criteria of 10^{-4} eV and 0.01 eV/Å were satisfied. Both atomic positions and lattice parameters were fully relaxed. Based on the optimized ground state structure, AIMD simulations were conducted in the canonical (NVT) ensemble for 5 ps with a time step of 1 fs, using a Nose-Hoover chain thermostat to maintain a temperature of 300 K.[47] Atomic configurations were sampled from the final 2 ps of the trajectories for subsequent calculations of time-dependent diabatic energies and electronic couplings.

Electronic couplings were evaluated using the POD method.[48,49] The system was partitioned into donor and acceptor fragments, each consisting of one inorganic Pb-Br layers and the associated four organic spacer cations (Figure 1). The Kohn-Sham Hamiltonian and overlap matrices in the atomic orbital basis were obtained using the OpenMX package,[50,51] with basis sets of s^2p^1 (H), $s^2p^2d^1$ (C, N, F), and $s^3p^2d^2f^1$ (Br, Pb). The Hamiltonian was subsequently orthogonalized and partitioned into donor and acceptor subspaces. After diagonalizing each subspace and applying the corresponding unitary transformations, the off-diagonal Hamiltonian elements were identified as electronic couplings between donor and acceptor states. Hole transfer couplings were obtained from matrix elements between the highest occupied crystal orbitals (HOCOs), while electron transfer couplings were evaluated analogously using the lowest unoccupied crystal orbitals (LUCOs). The reorganization energy (λ) was determined directly from the MD trajectory by computing the spectral density function of diabatic energy gap fluctuation within the linear response theory.[52,53] Further methodological details can be found in ref 32.

3. Results and Discussion

We first examine the crystal structural features of $(n\text{-BA})_2(MA)Pb_2Br_7$ (n-BA) and $(iso\text{-BA})_2(MA)Pb_2Br_7$ (iso-BA). The experimental crystal structures were adopted as the initial geometries,[54] and the optimized structures are shown in Figure S1. The calculated lattice constants are in good agreement with the experimental values (Table S1). Upon isomerization from *n*-BA to iso-BA, the lattice constant along the stacking direction decreases, consistent with a reduced interlayer spacing

from 7.21 Å to 6.45 Å (Figure 2a,b). This contraction can be attributed to the shorter effective chain length of the branched spacer cation. In addition, the inorganic $[PbBr_6]^{4-}$ octahedra in the iso-BA system exhibit more pronounced tilting relative to the stacking direction compared to the *n*-BA counterpart. The distortion of the $[PbBr_6]^{4-}$ octahedra can be quantified by the Pb–Br–Pb bond angles, where larger deviations from the ideal 180° indicate stronger distortion. In $n = 2$ RP perovskites, two types of Pb–Br–Pb angles are present: axial (perpendicular to the organic layers) and equatorial (within the inorganic plane). As shown in Figure 2c,d, the axial Pb–Br–Pb angle in the iso-BA system (~170.8°) is smaller than that in *n*-BA (~174.5°), indicating enhanced out-of-plane distortion. In contrast, the equatorial angle in iso-BA (~152.4°) is larger than that in *n*-BA (~147.8°), suggesting reduced in-plane distortion. The enhanced out-of-plane distortion in the iso-BA system originated from the strengthened hydrogen-bonding interactions between the organic cations and the inorganic framework, as evidenced by the shorter N–H···Br (axial) distances (Figure 2c,d). Conversely, the reduced in-plane distortion is accompanied by weaker hydrogen bonding between NH_3^+ groups and equatorial Br atoms, as well as an increased penetration depth, defined as the vertical distance between the nitrogen atom of the NH_3^+ group and the nearest terminal Br atom of the adjacent inorganic layer. This behavior arises because stronger interactions with terminal Br atoms pull the spacer cations away from the bridging Br sites. Since the band edge states in 2D RP perovskites are primarily dominated by the inorganic framework, these structural variations are expected to directly influence the electronic structure and play a critical role in governing charge transport.

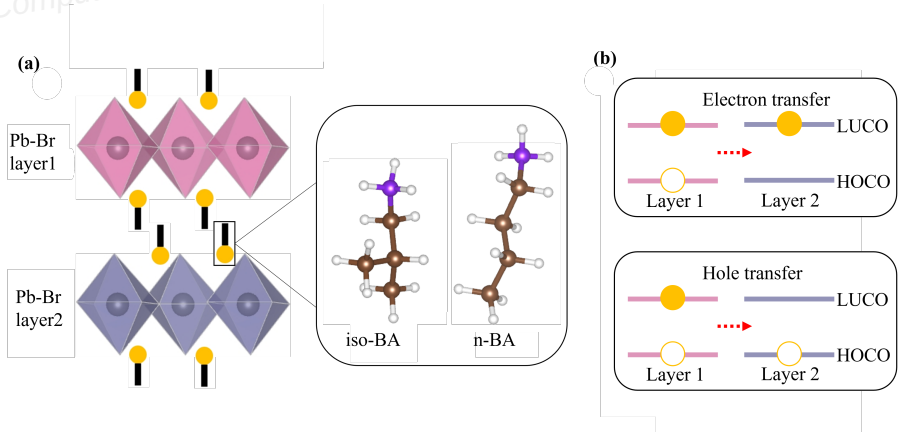

Figure 1. (**a**) Schematic illustration of the crystal structures of $(n\text{-BA})_2(MA)Pb_2Br_7$ (*n*-BA) and isomeric $(iso\text{-BA})_2(MA)Pb_2Br_7$ (iso-BA). Each crystalline model comprises two inorganic Pb–Br layers (layer 1 and layer 2), which are depicted in pink and purple, respectively. (**b**) Schematic depiction of the interlayer hole and electron transport. The interlayer charge transfer involves the migration of a photoexcited electron (or hole) from the LUCO (or HOCO) of one layer to the corresponding LUCO (or HOCO) of the adjacent layer.

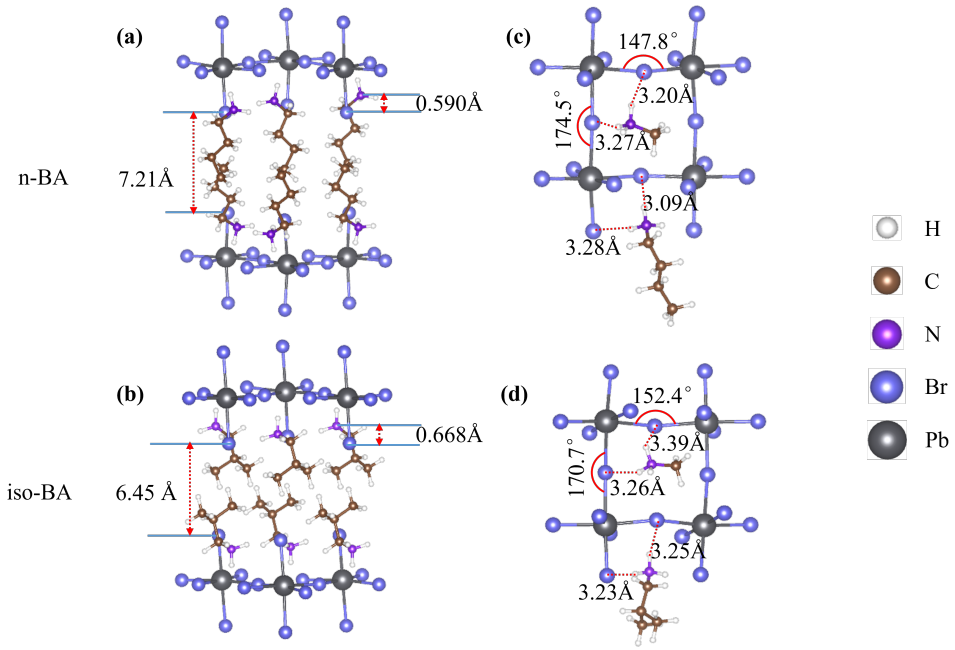

Figure 2. Key structural parameters in the n-BA and iso-BA systems. (**a, b**) Interlayer distance, characterized by the vertical Br···Br distance, and the penetration depth of organic cations, defined as the vertical distance between the nitrogen atom of -NH_3 group and the terminal Br atom. (**c, d**) Hydrogen bonds formed between the organic and inorganic components.

The nature of noncovalent interactions between the organic cations and the inorganic Pb–Br framework was analyzed using the noncovalent interaction (NCI) index, as developed by Johnson et al.[55] In this approach, the reduced density gradient (RDG) is plotted as a function of sign(λ_2)ρ, where λ_2 is the second eigenvalue of the Hessian matrix of the electron density (ρ). Figure 3a,b presents the 2D RDG plots, in which the blue region (sign(λ_2)ρ < 0) corresponds to attractive interactions (e.g., hydrogen bonding), the red region (sign(λ_2)ρ > 0) indicates strong repulsive interactions (e.g., steric effects), and the green region (sign(λ_2)ρ ≈ 0) represents weak van der Waals interactions. The corresponding 3D RDG isosurfaces (Figure 3c,d) provide spatial visualization of these interactions. As shown in Figures 3a,b, the RDG plot of *n*-BA exhibits more pronounced and left-shifted spikes in the range of −0.05 < sign(λ_2)ρ < −0.02 compared to the iso-BA system, indicating overall stronger attractive interactions in the *n*-BA structure. Consistently, the 3D isosurfaces reveal more prominent interaction regions between the ammonium hydrogen atoms and the Br atoms of the inorganic lattice in *n*-BA, confirming stronger N–H···Br hydrogen bonding in the linear spacer system relative to the branched analogue. The weakened noncovalent interactions in the iso-BA system lead to a softer lattice and enhanced thermal fluctuations at finite temperature compared to *n*-BA, which is expected to influence the diabatic energy level fluctuations and charge transport properties.

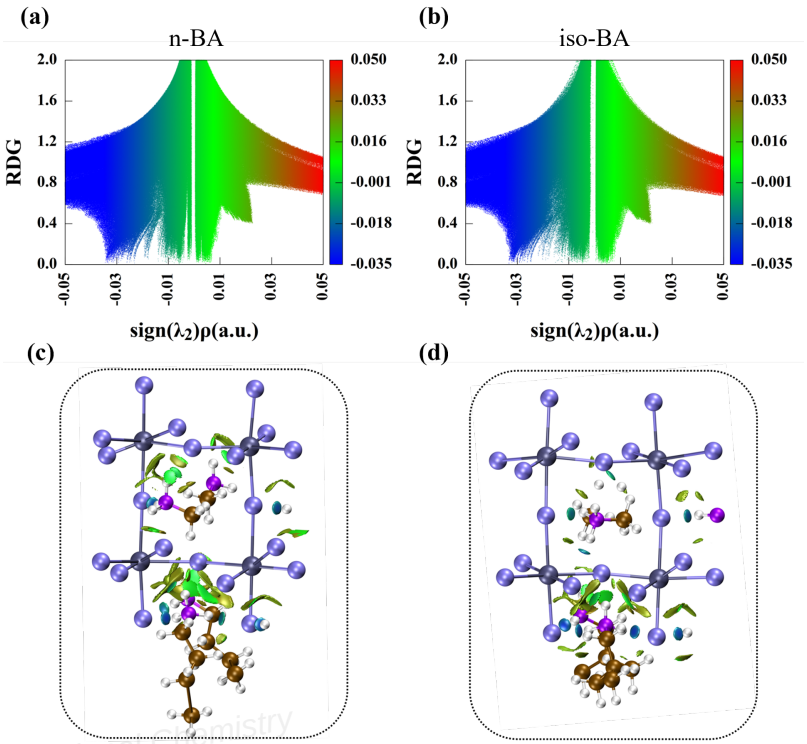

Figure 3. Non-covalent interaction (NCI) analysis. 2D reduced density gradient (RDG) plots as a function of sign(λ_2)ρ for (**a**) n-BA and (**b**) iso-BA, and corresponding 3D NCI isosurfaces are shown in (**c**) and (**d**), where blue, green, and red regions denote strong attractive, weak-to-moderate, and repulsive interactions, respectively.

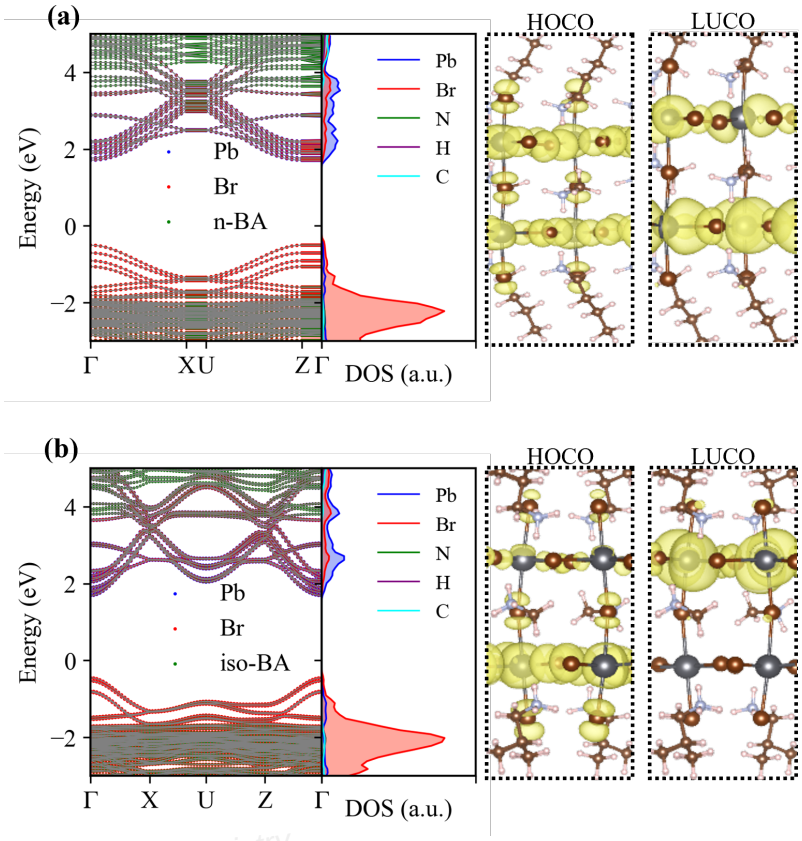

Figure 4. Electronic band structures and partial density of states (PDOS) for n-BA (**a**) and iso-BA systems (**b**). The right panels show the charge density distribution of LUCO and HOCO. For clarity, only one Pb–Br layer together with the organic spacer cations is displayed.

Figure 4 presents the partial density of states (PDOS) and electronic band structures of the systems under investigations. The highest occupied crystal orbital (HOCO) is primarily derived from antibonding interactions between Pb 6*s* and Br 4*p* orbitals, with dominant contributions from Br 4*p* states. The lowest unoccupied crystal orbital (LUCO) originates from hybridization between Pb 6*p* and Br 4*p* orbitals, with the nonbonding Pb 6*p* states playing a predominant role. The organic spacer cations do not directly contribute to the band edge states, but instead modulate the electronic properties of the inorganic framework through electrostatic interactions and hydrogen bonding. As shown in Figure 4a,b, both *n*-BA and iso-BA systems exhibit direct bandgaps, with the HOCO and LUCO located at the Γ point of the first Brillouin zone. The calculated bandgap of the *n*-BA system is approximately 2.2 eV, slightly larger than that of the iso-BA counterpart (2.1 eV). The highest occupied molecular orbital (HOMO) and lowest unoccupied molecular orbital (LUMO) levels of the spacer cations lie below the HOCO and above the LUCO of the inorganic Pb–Br framework, respectively, resulting in a type-I band alignment. The charge density distributions of the HOCO and LUCO are shown in the right panel of Figure 4. In the iso-BA system, the contribution of terminal (axial) Br atoms to the HOCO is reduced compared to the *n*-BA case. In addition, both HOCO and LUCO exhibit stronger localization in the iso-BA structure, as further supported by the inverse

participation ratio (IPR) values summarized in Table S2. This increased localization can be attributed to the enhanced out-of-plane octahedral distortion, which breaks structural symmetry and promotes carrier localization.

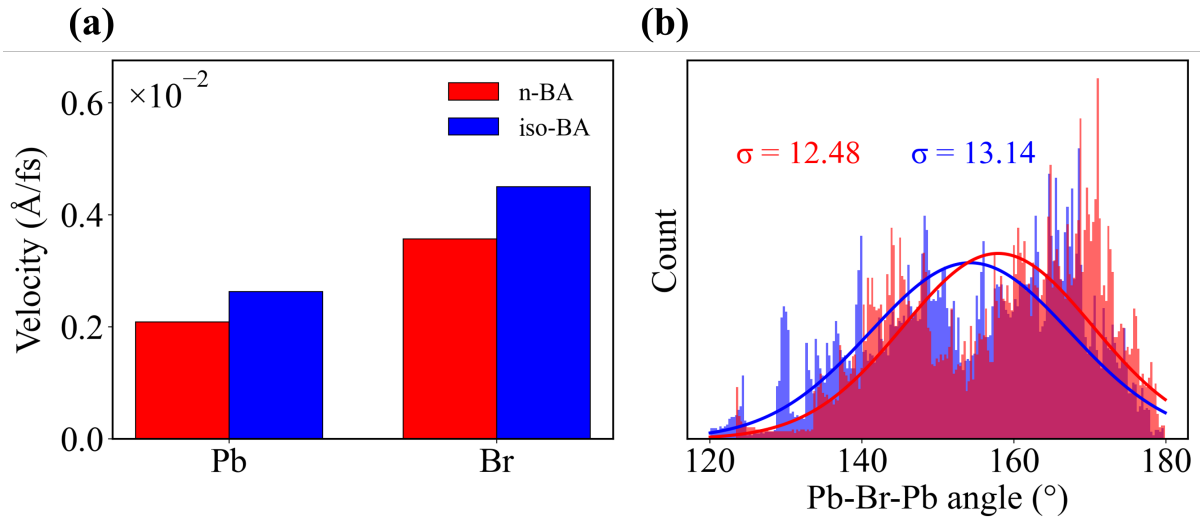

Figure 5. (**a**) Element-resolved root-mean-square velocity from 2 ps MD trajectories for the iso-BA (blue) and n-BA (red) systems. (**b**) Histogram distributions of Pb-Br-Pb bond angles, with the corresponding standard deviation (σ) of the bond angle fluctuations indicated.

We next turn to the structural dynamics at finite temperature. To quantify thermal fluctuations, we computed the atomic root-mean-square (RMS) velocities from the AIMD trajectories, as shown in Figure 5. The results indicate that the heaviest Pb atoms exhibit the smallest fluctuations, followed by Br atoms, whereas the light organic spacer components display the largest amplitudes of motion. Notably, in the iso-BA system, the RMS velocities of Pb and Br atoms are consistently higher than those in the *n*-BA counterpart, indicating enhanced lattice dynamics induced by carbon-chain isomerism. This behavior originates from the weakened N–H···Br hydrogen bonding between the NH_3^+ group and equatorial Br atoms at the organic–inorganic interface in the iso-BA structure, which reduces the structural constraints on the Pb–Br framework and thus facilitates larger atomic displacements. The enhanced lattice fluctuations directly modulate the electronic structure, particularly the band-edge states, through variations in the Pb–Br–Pb bond angles. To quantify this effect, we extracted the time-dependent Pb–Br–Pb angles along the AIMD trajectories (Figure 5b). As expected, the iso-BA system exhibits larger angular fluctuations than the *n*-BA structure, with a standard deviation increased by ~0.66°, consistent with the stronger atomic motions of Pb and Br. Given that the band-edge states are predominantly derived from Pb and Br atomic orbitals, such structural dynamics have direct implications for diabatic energy fluctuations and, consequently, charge transport. Figure 6 shows the time evolution of diabatic HOCO and LUCO energies for each layer at 300 K. Both exhibit pronounced fluctuations, with standard deviations in the range of 0.14–0.28 eV, reflecting strong electron–phonon coupling driven by intra-layer lattice dynamics. In general, the HOCO exhibits larger fluctuations than the LUCO, because it originates from antibonding Pb 6*s*–Br 4*p* interactions and is therefore more sensitive to variations in the Pb–Br–Pb angle, whereas the LUCO is mainly derived from nonbonding Pb 6*p* states. Consistent with the enhanced lattice dynamics, the iso-BA

system exhibits stronger diabatic energy fluctuations than the *n*-BA counterpart. Within the classical linear response framework, the reorganization energy is directly proportional to the variance of these energy fluctuations via:[32] $\lambda = \frac{\sigma_E^2}{2k_BT}$, where σ_E represents the standard deviation of the diabatic energy gap fluctuations between donor and acceptor states along the AIMD trajectory. Specifically, σ_E^2 is defined as: $\sigma E^2 = \langle(\delta\Delta E)^2\rangle_M$, $\delta\Delta E(t) = \Delta E(t) - \langle\Delta E\rangle_M$. The resulting reorganization energy, summarized in Table 1, show that iso-BA possesses a moderately larger reorganization energy, as expected.

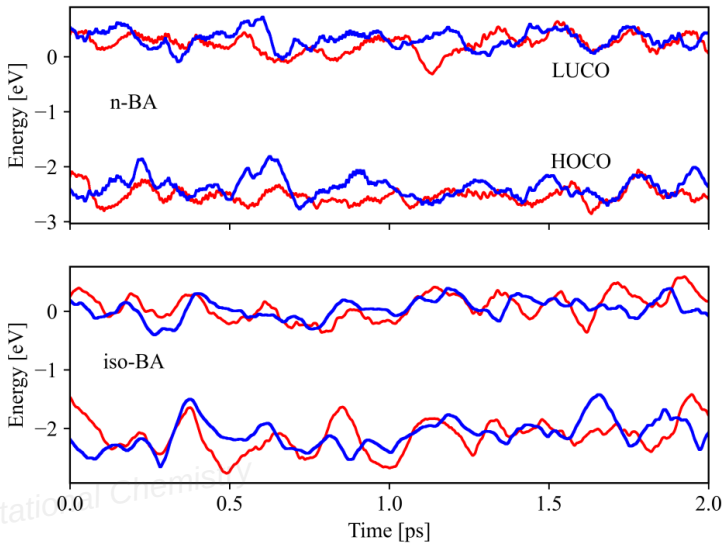

Figure 6. The time-evolution of HOCO and LUCO energy levels for layer 1 (red) and layer 2 (blue) in the n-BA and iso-BA systems.

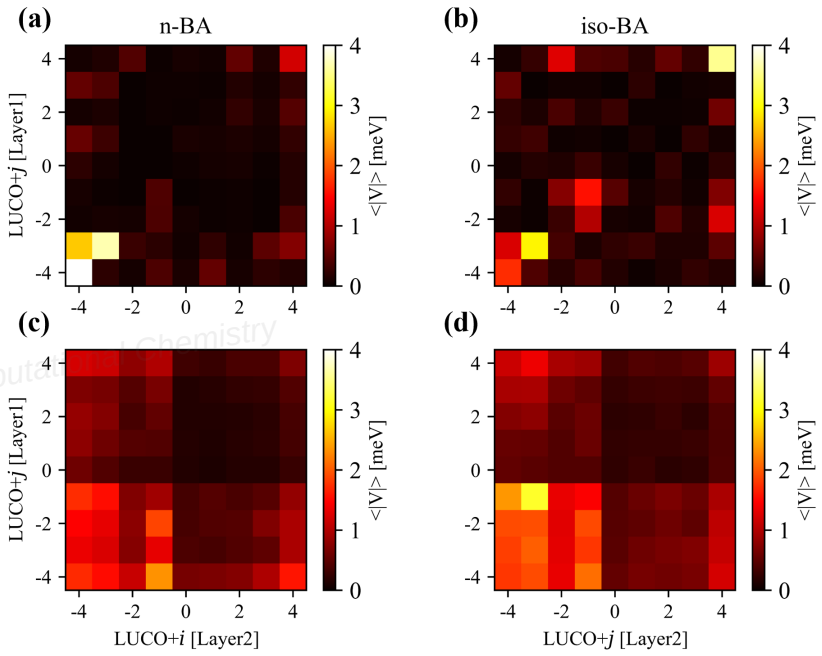

Figure 7. 2D maps of the canonical averaged values of absolute electronic couplings for the n-BA and iso-BA system at 0 K (top) and 300 K (bottom).

Table1. Canonically averaged absolute electronic couplings ($\langle V_{kl}^2\rangle^{1/2}$); reorganization energy (λ); hole and electron hopping time obtained from the semiclassical Marcus theory (τ_{Marcus}), and the carrier mobility calculated based on the Marcus hopping rate (μ_{hop}).

		$\langle V_{kl}^2\rangle^{1/2}$ (meV)	λ (eV)	τ_{Marcus} (μs)	μ_{hop} ($cm^2V^{-1}s^{-1}$)
n-BA	HOCO-HOCO	1.10	1.34	22.58	8.91×10^{-9}
	LUCO-LUCO	0.116	1.05	110.6	1.82×10^{-9}
iso-BA	HOCO-HOCO	2.86	1.38	4.98	3.23×10^{-8}
	LUCO-LUCO	0.332	1.12	27.33	5.89×10^{-9}

Figure 7 presents 2D maps of averaged absolute values of electronic coupling. Each grid point corresponds to the averaged magnitude of the coupling between a pair of states in adjacent layers, providing an intuitive representation of interlayer electronic interactions. The coupling strength is governed by the overlap between donor and acceptor wavefunctions, which depends sensitively on structural factors such as interlayer spacing, given the exponential decay dependence of wavefunction overlap with donor-acceptor separation. The results indicate that interlayer electronic couplings are generally weak, on the order of 10^{-4} to 10^{-3} eV. At 0 K, the coupling matrix exhibits a nearly symmetric distribution, reflecting the structural equivalence of the two Pb–Br layers. At 300 K, thermal fluctuations break this symmetry, leading to an asymmetric distribution and a noticeable enhancement in the overall coupling strength. Notably, hole transfer couplings are one order of magnitude larger than electron transfer couplings (Table 1). This difference originates from the distinct orbital characters at the band edges: the CBM is dominated by localized, nonbonding Pb 6*p* orbitals, whereas the VBM arises from antibonding hybridization between Pb 6*s* and Br 4*p* orbitals. As a result, the VBM is more sensitive to lattice fluctuations, enabling transient wavefunction delocalization that enhances electronic coupling. Furthermore, the iso-BA system exhibits significantly stronger electronic couplings than the *n*-BA counterpart. This enhancement primarily stems from the reduced interlayer spacing associated with the shorter effective carbon chain in the branched spacer. Although the iso-BA system shows reduced contributions from terminal Br atoms to the band edge states and increased charge localization due to stronger out-of-plane octahedral distortion, the shortened interlayer distance increases donor–acceptor wavefunction overlap, ultimately strengthening the coupling. Overall, the carbon-chain isomerism induced enhancement of electronic coupling is expected to facilitate more efficient out-of-plane charge transport in 2D perovskites.

Finally, we evaluated the Marcus charge transfer rates for the *n*-BA and iso-BA systems using the computed electronic couplings and reorganization energies as inputs. The results are summarized in Table 1. It should be noted that the the electronic coupling entering the Marcus rate expression is defined as $\langle V^2\rangle^{1/2}$. The simulations show that the hole and electron hopping times in the iso-BA system are approximately 4.98 and 27.33 μs, respectively, corresponding to out-of-plane carrier mobilities on the order of 10^{-8} and 10^{-9} $cm^2V^{-1}s^{-1}$. These values are about a few times higher than those in the *n*-BA system, in agreement with the experimental trend reported by chen et al.[54] The difference in charge transfer rate between *n*-BA and iso-BA can be rationalized by the interplay between

electronic coupling and reorganization energy. The reduced interlayer spacing in the iso-BA system enhances wavefunction overlap between adjacent inorganic layers, leading to significantly stronger electronic coupling. Meanwhile, the weaker hydrogen-bonding interactions in the isomeric structure promote larger thermal fluctuations of Pb and Br atoms, resulting in a moderate increase in the reorganization energy. Consequently, the gain in electronic coupling outweighs the increase in reorganization energy, giving rise to markedly faster out-of-plane charge transport. In addition, hole transfer is consistently faster than electron transfer across both systems, owing to the substantially larger electronic couplings associated with valence-band states. Overall, these results demonstrate that carbon-chain isomerism of organic spacer cations provides an effective strategy to enhance interlayer charge transfer, offering valuable design principles for optimizing vertical carrier transport in 2D RP perovskites.

4. Conclusion

In summary, we have investigated how carbon-chain isomerism of organic spacer cations modulates out-of-plane charge transport in 2D RP perovskites using a first-principles framework that integrates *ab initio* molecular dynamics, projection-operator diabatization, and semiclassical Marcus theory. By comparing systems with linear *n*-BA and branched iso-BA spacers, we show that isomerization from a linear to a branched chain enhances both electron and hole mobilities by approximately three- to fourfold, in qualitative agreement with experimental observations. Mechanistically, iso-BA spacers preferentially orient toward terminal Br atoms and away from bridging Br sites, weakening the overall hydrogen-bonding interactions at the organic–inorganic interface. This reduced constraint increases the flexibility of the Pb–Br framework, leading to enhanced thermal fluctuations of Pb and Br atoms and, consequently, stronger diabatic energy fluctuations of the HOCO and LUCO levels. As a result, the reorganization energy increases moderately by several tens of meV. In parallel, the shorter effective chain length of iso-BA reduces the interlayer spacing, which enhances interlayer electronic coupling by approximately threefold. The gain in electronic coupling outweighs the modest increase in reorganization energy, resulting in significantly accelerated charge transport in the iso-BA system. Additionally, thermally induced lattice fluctuations promote transient wavefunction delocalization, further increasing donor–acceptor orbital overlap and electronic coupling. Consequently, the iso-BA system achieves higher hole and electron mobilities on the order of 10^{-9} - 10^{-8} $cm^2V^{-1}s^{-1}$, respectively, surpassing those of the *n*-BA counterpart. Overall, these findings establish carbon-chain isomerism as a chemically simple yet powerful strategy for enhancing interlayer charge transport in 2D layered perovskites, providing valuable design principles for high-performance optoelectronic devices.

Acknowledgements

W. L. acknowledges financial support of National Natural Science Foundation of China (grant No. 22373033).

Supporting Information

Optimized ground-state structures; comparison of experimental and calculated lattice constants;

inverse participation ratio analysis of HOCO and LUCO states.

REFERENCES

(1) Li, G.; Zhang, Z.; Agyei-Tuffour, B.; Wu, L.; Gries, T. W.; Prashanthan, K.; Frohloff, L.; Musiienko, A.; Li, J.; Zhu, R.; Hart, L. J. F.; Wang, L.; Li, Z.; Hou, B.; Koch, N.; Saba, M.; Barnes, P. R. F.; Nelson, J.; Dyson, P. J.; Nazeeruddin, M. K.; Li, M.; Abate, A. Stabilizing High-Efficiency Perovskite Solar Cells via Strategic Interfacial Contact Engineering. *Nat. Photon.* **2026**, *20* (1), 55–62. https://doi.org/10.1038/s41566-025-01791-1.

(2) Xiong, Z.; Zhang, Q.; Cai, K.; Zhou, H.; Song, Q.; Han, Z.; Kang, S.; Li, Y.; Jiang, Q.; Zhang, X.; others. Homogenized Chlorine Distribution For> 27% Power Conversion Efficiency in Perovskite Solar Cells. *Science* **2025**, *390* (6773), 638–642.

(3) Castriotta, L. A.; Wang, M.; Shi, X.; Dou, B. D.; Schelhas, L. T.; Huang, J. Challenges, Technological Pathways and Trade-Offs of Perovskite Solar Modules for Long-Term Operation. *Nature Energy* **2026**, 1–13.

(4) Boyd, C. C.; Cheacharoen, R.; Leijtens, T.; McGehee, M. D. Understanding Degradation Mechanisms and Improving Stability of Perovskite Photovoltaics. *Chemical reviews* **2018**, *119* (5), 3418–3451.

(5) Zhou, Y.; Zhao, Y. Chemical Stability and Instability of Inorganic Halide Perovskites. *Energy & environmental science* **2019**, *12* (5), 1495–1511.

(6) Pereira, M.; Martins, J.; Madureira, R.; Ivanou, D.; Emami, S.; Mendes, A. Light Stability of Laser-Assisted Glass Encapsulated Perovskite Solar Cells under Different Atmospheres. *Advanced Energy Materials* **2026**, e06288.

(7) Sun, K.; Guo, R.; Zhou, Q.; Fang, L.; Jiang, X.; Wegener, S. A.; Liang, Y.; Li, Z.; Liang, S.; Schwartzkopf, M.; others. Insights into the Operational Stability of Wide-Bandgap Perovskite and Tandem Solar Cells under Rapid Thermal Cycling. *Nature Communications* **2026**.

(8) Kore, B. P.; Jamshidi, M.; Gardner, J. M. The Impact of Moisture on the Stability and Degradation of Perovskites in Solar Cells. *Materials Advances* **2024**, *5* (6), 2200–2217.

(9) Park, B.; Seok, S. I. Intrinsic Instability of Inorganic–Organic Hybrid Halide Perovskite Materials. *Advanced Materials* **2019**, *31* (20), 1805337.

(10) Conings, B.; Drijkoningen, J.; Gauquelin, N.; Babayigit, A.; D'Haen, J.; D'Olieslaeger, L.; Ethirajan, A.; Verbeeck, J.; Manca, J.; Mosconi, E.; others. Intrinsic Thermal Instability of Methylammonium Lead Trihalide Perovskite. *Advanced Energy Materials* **2015**, *5* (15), 1500477.

(11) Tsai, H.; Nie, W.; Blancon, J.-C.; Stoumpos, C. C.; Asadpour, R.; Harutyunyan, B.; Neukirch, A. J.; Verduzco, R.; Crochet, J. J.; Tretiak, S.; others. High-Efficiency Two-Dimensional Ruddlesden–Popper Perovskite Solar Cells. *Nature* **2016**, *536* (7616), 312–316.

(12) Grancini, G.; Nazeeruddin, M. K. Dimensional Tailoring of Hybrid Perovskites for Photovoltaics. *Nature Reviews Materials* **2019**, *4* (1), 4–22.

(13) Liu, C.; Yang, Y.; Chen, H.; Spanopoulos, I.; Bati, A. S.; Gilley, I. W.; Chen, J.; Maxwell, A.; Vishal, B.; Reynolds, R. P.; others. Two-Dimensional Perovskitoids Enhance Stability in Perovskite Solar Cells. *Nature* **2024**, *633* (8029), 359–364.

(14) Zhang, X.; Ren, X.; Liu, B.; Munir, R.; Zhu, X.; Yang, D.; Li, J.; Liu, Y.; Smilgies, D.-M.; Li, R.; Yang, Z.; Niu, T.; Wang, X.; Amassian, A.; Zhao, K.; Liu, S. (Frank). Stable High Efficiency Two-Dimensional Perovskite Solar Cells via Cesium Doping. *Energy Environ. Sci.* **2017**, *10* (10), 2095–2102. https://doi.org/10.1039/C7EE01145H.

(15) Ren, M.; Cao, S.; Zhao, J.; Zou, B.; Zeng, R. Advances and Challenges in Two-Dimensional Organic–Inorganic Hybrid Perovskites Toward High-Performance Light-Emitting Diodes. *Nano-Micro Lett.* **2021**, *13* (1), 163.

https://doi.org/10.1007/s40820-021-00685-5.

(16) Cheng, P.; Wu, T.; Zhang, J.; Li, Y.; Liu, J.; Jiang, L.; Mao, X.; Lu, R.-F.; Deng, W.-Q.; Han, K. ($C_6 H_5 C_2 H_4 NH_3$)$_2$ GeI_4 : A Layered Two-Dimensional Perovskite with Potential for Photovoltaic Applications. *J. Phys. Chem. Lett.* **2017**, *8* (18), 4402–4406. https://doi.org/10.1021/acs.jpclett.7b01985.

(17) Dai, X.; Xu, K.; Wei, F. Recent Progress in Perovskite Solar Cells: The Perovskite Layer. *Beilstein J. Nanotechnol.* **2020**, *11*, 51–60. https://doi.org/10.3762/bjnano.11.5.

(18) Chen, Y.; Sun, Y.; Peng, J.; Tang, J.; Zheng, K.; Liang, Z. 2D Ruddlesden–Popper Perovskites for Optoelectronics. *Advanced Materials* **2018**, *30* (2), 1703487. https://doi.org/10.1002/adma.201703487.

(19) Dou, L.; Wong, A. B.; Yu, Y.; Lai, M.; Kornienko, N.; Eaton, S. W.; Fu, A.; Bischak, C. G.; Ma, J.; Ding, T.; others. Atomically Thin Two-Dimensional Organic-Inorganic Hybrid Perovskites. *Science* **2015**, *349* (6255), 1518–1521.

(20) Chen, S.; Shi, G. Two-Dimensional Materials for Halide Perovskite-Based Optoelectronic Devices. *Advanced Materials* **2017**, *29* (24), 1605448. https://doi.org/10.1002/adma.201605448.

(21) Ren, H.; Yu, S.; Chao, L.; Xia, Y.; Sun, Y.; Zuo, S.; Li, F.; Niu, T.; Yang, Y.; Ju, H.; others. Efficient and Stable Ruddlesden–Popper Perovskite Solar Cell with Tailored Interlayer Molecular Interaction. *Nature Photonics* **2020**, *14* (3), 154–163.

(22) Min, L.; Sun, H.; Guo, L.; Wang, M.; Cao, F.; Zhong, J.; Li, L. Frequency-Selective Perovskite Photodetector for Anti-Interference Optical Communications. *Nature Communications* **2024**, *15* (1), 2066.

(23) Wang, K.; Wu, C.; Yang, D.; Jiang, Y.; Priya, S. Quasi-Two-Dimensional Halide Perovskite Single Crystal Photodetector. *ACS nano* **2018**, *12* (5), 4919–4929.

(24) Tan, Z.; Wu, Y.; Hong, H.; Yin, J.; Zhang, J.; Lin, L.; Wang, M.; Sun, X.; Sun, L.; Huang, Y.; others. Two-Dimensional (C4H9NH3) 2PbBr4 Perovskite Crystals for High-Performance Photodetector. *Journal of the American Chemical Society* **2016**, *138* (51), 16612–16615.

(25) Lanzetta, L.; Marin-Beloqui, J. M.; Sanchez-Molina, I.; Ding, D.; Haque, S. A. Two-Dimensional Organic Tin Halide Perovskites with Tunable Visible Emission and Their Use in Light-Emitting Devices. *ACS Energy Letters* **2017**, *2* (7), 1662–1668.

(26) Kareem, M.; Salih, E. Y.; Nayak, P. P.; Sundharam, S.; Kumar, S.; others. Exploring Performance Limits toward 20.79% Efficiency in 2D-Layered Ruddlesden–Popper Perovskite Solar Cells. *Energy Advances* **2026**.

(27) Tang, Y.; Dong, X.; Li, X.; Zhou, Y.; Ran, C.; Wu, Z. Two-Dimensional Ruddlesden-Popper Perovskite Solar Cells with an Efficiency Exceeding 19 % by Inserting a Self-Assembled Monolayer. *Chemical Engineering Journal* **2024**, *499*, 156503. https://doi.org/10.1016/j.cej.2024.156503.

(28) Shao, M.; Bie, T.; Yang, L.; Gao, Y.; Jin, X.; He, F.; Zheng, N.; Yu, Y.; Zhang, X. Over 21% Efficiency Stable 2D Perovskite Solar Cells. *Advanced Materials* **2022**, *34* (1), 2107211. https://doi.org/10.1002/adma.202107211.

(29) Fu, Q.; Chen, M.; Li, Q.; Liu, H.; Wang, R.; Liu, Y. Selenophene-Based 2D Ruddlesden-Popper Perovskite Solar Cells with an Efficiency Exceeding 19%. *J. Am. Chem. Soc.* **2023**, *145* (39), 21687–21695. https://doi.org/10.1021/jacs.3c08604.

(30) Li, X.; Dong, X.; Shen, Z.; Zai, X.; Li, Y.; Miao, Z.; Song, L.; Wu, Z. Halogenated Chiral Organic Spacer Cation Regulation for Efficient and Stable 2D Ruddlesden-Popper Perovskite Solar Cells. *Adv Funct Materials* **2025**, *35* (45), 2507591. https://doi.org/10.1002/adfm.202507591.

(31) Rodrigues, M. H. de M.; Sobrinho, J. A.; Machado, A. P.; Brandao, Z. C.; Barcelos, I. D.; Labre, C.; Szostak, R.; Nogueira, A. F. Tuning Structure and Performance of 2D/3D Perovskites by Alkyl Chain Length Engineering. *ACS Energy Letters* **2026**.

(32) Li, W.; Giannini, S.; Quarti, C.; Hou, Z.; Prezhdo, O. V.; Beljonne, D. Interlayer Charge Transport in 2D Lead

Halide Perovskites from First Principles. *J. Chem. Theory Comput.* **2023**, *19* (24), 9403–9415. https://doi.org/10.1021/acs.jctc.3c00904.

(33) Quan, J.; Yu, S.; Xing, B.; He, X.; Zhang, L. Two-Dimensional Ruddlesden-Popper Halide Perovskite Solar Absorbers with Short-Chain Interlayer Spacers. *Physical Review Materials* **2022**, *6* (6), 065405.

(34) Ge, Z.; Cao, H.; Feng, Q.; Li, W.; Chen, J.; Nan, G. Influences of Inorganic Sublattice Stacking on Out-of-Plane Charge Transport in Two-Dimensional Ruddlesden–Popper Perovskites: A First-Principles Study. *J. Phys. Chem. C* **2026**, *130* (14), 5332–5339. https://doi.org/10.1021/acs.jpcc.6c01475.

(35) Zhang, F.; Kim, D. H.; Lu, H.; Park, J.-S.; Larson, B. W.; Hu, J.; Gao, L.; Xiao, C.; Reid, O. G.; Chen, X.; others. Enhanced Charge Transport in 2D Perovskites via Fluorination of Organic Cation. *Journal of the American Chemical Society* **2019**, *141* (14), 5972–5979.

(36) Shi, J.; Gao, Y.; Gao, X.; Zhang, Y.; Zhang, J.; Jing, X.; Shao, M. Fluorinated Low-Dimensional Ruddlesden–Popper Perovskite Solar Cells with over 17% Power Conversion Efficiency and Improved Stability. *Advanced Materials* **2019**, *31* (37), 1901673.

(37) Stippell, E.; Li, W.; Quarti, C.; Beljonne, D.; Prezhdo, O. V. Enhancing Interlayer Charge Transport of Two-Dimensional Perovskites by Structural Stabilization via Fluorine Substitution. *ACS Appl. Mater. Interfaces* **2025**, *17* (1), 2032–2040. https://doi.org/10.1021/acsami.4c17876.

(38) Cheng, B.; Li, T.-Y.; Wei, P.-C.; Yin, J.; Ho, K.-T.; Retamal, J. R. D.; Mohammed, O. F.; He, J.-H. Layer-Edge Device of Two-Dimensional Hybrid Perovskites. *Nature communications* **2018**, *9* (1), 5196.

(39) Ribeiro, I. C.; Picoli, F. D.; Moraes, P. I. R.; Fonseca, A. F. V.; Oliveira, L. N.; Nogueira, A. F.; Da Silva, J. L. F. Impact of Thin Film Thickness on the Structural, Energetic and Optoelectronic Properties of Two-Dimensional $FPEA_2(MA_{n-1})Pb_nI_{3n+1}$ Perovskites. *ACS Appl. Energy Mater.* **2025**, *8* (6), 3346–3359. https://doi.org/10.1021/acsaem.4c02800.

(40) Li, W.; Zhang, P.; Kong, D.; Zhou, L.; Stippell, E.; Beljonne, D.; Prezhdo, O. V. Ab Initio Nonadiabatic Molecular Dynamics in Weakly Coupled Nanosystems. *Journal of Chemical Theory and Computation* **2025**, *21* (24), 12453–12465.

(41) Kresse, G.; Furthmüller, J. Efficiency of Ab-Initio Total Energy Calculations for Metals and Semiconductors Using a Plane-Wave Basis Set. *Computational materials science* **1996**, *6* (1), 15–50.

(42) Kresse, G.; Furthmüller, J. Efficient Iterative Schemes for Ab Initio Total-Energy Calculations Using a Plane-Wave Basis Set. *Physical review B* **1996**, *54* (16), 11169.

(43) Ernzerhof, M.; Scuseria, G. E. Assessment of the Perdew–Burke–Ernzerhof Exchange-Correlation Functional. *The Journal of chemical physics* **1999**, *110* (11), 5029–5036.

(44) Hammer, B.; Hansen, L. B.; Nørskov, J. K. Improved Adsorption Energetics within Density-Functional Theory Using Revised Perdew-Burke-Ernzerhof Functionals. *Physical review B* **1999**, *59* (11), 7413.

(45) Perdew, J. P.; Burke, K.; Ernzerhof, M. Generalized Gradient Approximation Made Simple. *Phys. Rev. Lett.* **1996**, *77* (18), 3865–3868. https://doi.org/10.1103/PhysRevLett.77.3865.

(46) Grimme, S.; Antony, J.; Ehrlich, S.; Krieg, H. A Consistent and Accurate Ab Initio Parametrization of Density Functional Dispersion Correction „DFT-D… for the 94 Elements H-Pu. **2026**.

(47) Martyna, G. J.; Klein, M. L.; Tuckerman, M. Nosé–Hoover Chains: The Canonical Ensemble via Continuous Dynamics. *The Journal of chemical physics* **1992**, *97* (4), 2635–2643.

(48) Futera, Z.; Blumberger, J. Electronic Couplings for Charge Transfer across Molecule/Metal and Molecule/Semiconductor Interfaces: Performance of the Projector Operator-Based Diabatization Approach. *The Journal of Physical Chemistry C* **2017**, *121* (36), 19677–19689.

(49) Kondov, I.; Čížek, M.; Benesch, C.; Wang, H.; Thoss, M. Quantum Dynamics of Photoinduced Electron-Transfer Reactions in Dye- Semiconductor Systems: First-Principles Description and Application to Coumarin

343- TiO2. *The Journal of Physical Chemistry C* **2007**, *111* (32), 11970–11981.

(50) Ozaki, T. Variationally Optimized Atomic Orbitals for Large-Scale Electronic Structures. *Phys. Rev. B* **2003**, *67* (15), 155108. https://doi.org/10.1103/PhysRevB.67.155108.

(51) Ozaki, T.; Kino, H. Numerical Atomic Basis Orbitals from H to Kr. *Phys. Rev. B* **2004**, *69* (19), 195113. https://doi.org/10.1103/PhysRevB.69.195113.

(52) Oberhofer, H.; Reuter, K.; Blumberger, J. Charge Transport in Molecular Materials: An Assessment of Computational Methods. *Chem. Rev.* **2017**, *117* (15), 10319–10357. https://doi.org/10.1021/acs.chemrev.7b00086.

(53) Hsu, C.-P. Reorganization Energies and Spectral Densities for Electron Transfer Problems in Charge Transport Materials. *Phys. Chem. Chem. Phys.* **2020**, *22* (38), 21630–21641. https://doi.org/10.1039/D0CP02994G.

(54) Chen, Y.; Sun, Y.; Peng, J.; Zhang, W.; Su, X.; Zheng, K.; Pullerits, T.; Liang, Z. Tailoring Organic Cation of 2D Air-Stable Organometal Halide Perovskites for Highly Efficient Planar Solar Cells. *Advanced Energy Materials* **2017**, *7* (18), 1700162. https://doi.org/10.1002/aenm.201700162.

(55) Johnson, E. R.; Keinan, S.; Mori-Sánchez, P.; Contreras-García, J.; Cohen, A. J.; Yang, W. Revealing Noncovalent Interactions. *J. Am. Chem. Soc.* **2010**, *132* (18), 6498–6506. https://doi.org/10.1021/ja100936w.

Communications in Computational Chemistry